ELECTROCHEMISTRY

In situ formation of molecular Ni-Fe active sites on heteroatom-doped graphene as a heterogeneous electrocatalyst toward oxygen evolution

Jiong Wang,[1] Liyong Gan,[2] Wenyu Zhang,[1] Yuecheng Peng,[1] Hong Yu,[3] Qingyu Yan,[3] Xinghua Xia,[4] Xin Wang[1]*

Molecularly well-defined Ni sites at heterogeneous interfaces were derived from the incorporation of Ni^{2+} ions into heteroatom-doped graphene. The molecular Ni sites on graphene were redox-active. However, they showed poor activity toward oxygen evolution reaction (OER) in KOH aqueous solution. We demonstrated for the first time that the presence of Fe^{3+} ions in the solution could bond at the vicinity of the Ni sites with a distance of 2.7 Å, generating molecularly sized and heterogeneous Ni-Fe sites anchored on doped graphene. These Ni-Fe sites exhibited markedly improved OER activity. The Pourbaix diagram confirmed the formation of the Ni-Fe sites and revealed that the Ni-Fe sites adsorbed HO^- ions with a bridge geometry, which facilitated the OER electrocatalysis.

INTRODUCTION

Electrochemical or photoelectrochemical water splitting to generate hydrogen (H_2) and oxygen (O_2) is a promising strategy to convert intermittent renewable energies, such as sunlight, wind, and hydropower, into storable chemical fuels (*1*–*3*). Oxygen evolution reaction (OER), which occurs at the cathode in the process of water splitting, exhibits slow kinetics and thus limits the overall efficiency of this energy conversion. IrO_2 and RuO_2 are the benchmark OER catalysts with appreciable turnover frequencies (TOFs) at moderate overpotentials (η). However, the high cost and scarcity of these catalysts limit their wide applications (*4*, *5*). Many efforts have been endeavored to explore inexpensive and highly active OER catalysts. Molecular electrocatalysts are a promising candidate because of their high specific catalytic activity and selectivity. Molecular catalysts, such as transition metal complexes (*6*), redox-active organics (*7*), and enzymes (*8*), are usually synthesized with earth-abundant elements and have been developed for various catalytic reactions. The spatial arrangement of their active sites is molecularly well-defined, allowing them to be systematically tuned to optimize their catalytic activity and selectivity (*9*–*12*). Molecular catalysis is usually performed in homogeneous solutions, so that the active sites can be fully exposed and used for catalysis. However, these homogeneous solutions make it difficult to recover the molecular catalysts from the reaction media with intact structures (*13*, *14*). In addition, many molecular catalysts are dissolvable, stable, or active only in nonaqueous media (*15*, *16*). They cannot be easily integrated into water (photo)-electrolysis devices, where aqueous electrolytes are used for practical applications (*17*). To address these challenges, one appealing idea is to immobilize molecular catalysts onto the surfaces of heterogeneous solid matrices.

Several recent works were carried out to immobilize molecular catalysts onto the surfaces of the solid matrices through either covalent (*11*, *18*) or noncovalent (*19*–*21*) linkages. These heterogenized molecular catalysts were proved to be active to the catalytic reactions, for example, H_2 evolution (*17*, *18*) and CO_2 reduction (*16*, *21*) in aqueous solutions. Among these studies, carbonaceous materials were the most popular solid matrices to load molecular catalysts because of their high surface area, high electronic conductivity, and good stability (*18*, *19*, *22*). For OER electrocatalysis, we previously developed a heteroatom-doped graphene (HG) to conjugate molecular Co^{2+} ions (*23*). The sulfoxide groups in HG were found to effectively bond with Co^{2+} ions through coordination under mild conditions. They also facilitated the electron transfer between the electrode and Co^{2+} sites, generating Co^{4+} species as active sites for OER. Here, we used HG as the solid matrices to conjugate molecular Ni^{2+} ions to graphene surfaces for OER in alkaline solutions (1 M KOH). The Ni sites on graphene exhibited clear redox features coupled with the transfer of HO^- ions. These Ni sites were demonstrated to be intrinsically inactive for OER. However, we found that structural evolution occurred at the molecular Ni sites in a KOH solution containing trace amounts of Fe, and the resulting molecular composite catalyst exhibited high activity and stability toward OER. Although this Ni-Fe synergistic effect has been reported on oxides/hydroxides containing Ni-Fe at bulk or at the nanoscale level, likely due to the tuning of the redox features of metal sites (*24*–*31*), for the first time at the molecular level, we demonstrated that on the OER-inert HG-Ni, the Fe species could bond at the vicinity of the Ni sites to form dual Ni-Fe sites with a distance of 2.7 Å. Coupled with HO^- ions through terminal and bridging geometries, these molecular sites were well dispersed at graphene interfaces and were active and stable for OER, which shed light on the development of molecular heterogeneous electrocatalysts.

RESULTS

Heterogenization of molecular Ni^{2+} ions

HG was synthesized from graphene oxides and thiourea in a previously developed hydrothermal method. The as-prepared HG contained sulfoxide groups that could be the main coordination sites for transition metal ions (*23*). $Ni(acac)_2$ provided Ni^{2+} ions, which interacted with HG under mild conditions and were immobilized on HG (denoted as HG-Ni; details are provided in Materials and Methods). The transmission electron microscope (TEM) images showed that the two-dimensional HG-Ni structures contained substantial wrinkles and scrolls, which were

[1]School of Chemical and Biomedical Engineering, Nanyang Technological University, 62 Nanyang Drive, Singapore 637459, Singapore. [2]School of Material Science and Engineering, Key Laboratory of Advanced Energy Storage Materials of Guangdong Province, South China University of Technology, Guangzhou 510641, China. [3]School of Materials Science and Engineering, Nanyang Technological University, 50 Nanyang Avenue, Singapore 639798, Singapore. [4]School of Chemistry and Chemical Engineering, Nanjing University, Nanjing 210046, China.
*Corresponding author. Email: wangxin@ntu.edu.sg

the characteristics of graphene (Fig. 1A and fig. S1). On the graphene layers, the crystal lattices of Ni oxides were not observed. However, energy-dispersive x-ray (EDX) spectroscopy indicated a clear and uniform distribution of Ni, implying that the Ni sites in HG-Ni could be at molecular scales (figs. S2 and S3). The Ni signal was not detected on the HG precursor by EDX.

Figure 1B presents the normalized Ni K-edge x-ray absorption spectroscopy (XAS) data of the $Ni(acac)_2$ precursor and HG-Ni. The inset shows the expanded pre-edge region. The relative intensity of the pre-edge peak is closely related to the local geometry of Ni sites (*32*, *33*). From $Ni(acac)_2$ to HG-Ni, the pre-edge peak of Ni sites only increased slightly, suggesting the similar coordination geometry of Ni sites in Ni $(acac)_2$ and HG-Ni. Because previous single-crystal x-ray diffraction measurements showed that $Ni(acac)_2$ has a distorted octahedral geometry (*34*), it was thus suggested to retain the distorted octahedral geometry of Ni sites in HG-Ni. Besides, the pre-edge energy shifted very slightly [~0.08 eV, from $Ni(acac)_2$ to HG-Ni], which also reflected the almost equivalent ligand field at the two Ni sites (*35*). Based on the rising-edge energy, the oxidation state of Ni sites (+2) in HG-Ni was barely altered. In the Fourier-transformed extended x-ray absorption fine structure (EXAFS; Fig. 1C) analysis, the bond length of the inner shell of Ni centers (that is, Ni–O bonds) showed a minor increase. However, the outer shell changed significantly based on the peak at a radial distance (R') of 2.68 Å, confirming the bonding of Ni^{2+} ions with HG (*23*). The conjugation process was also investigated by density functional theory (DFT) calculations. In a stable model (Fig. 1D), it was found that at the Ni center, four O-donor atoms of two acetylacetonate ligands occupied the equatorial plane. At the axial positions, the Ni center interacted with HG through the O atoms of the doped sulfoxide group, which thus enabled the immobilization of Ni^{2+} ions. The distance between the Ni atom and the O atom of the sulfoxide group was theoretically found to be 2.87 Å, which reflected the newly occurred peak (2.68 Å) in the HG-Ni EXAFS data. In addition, the Fourier transform infrared (FTIR; fig. S4) spectra exhibited a characteristic vibration of $Ni(acac)_2$ at 2990 cm^{-1}. This characteristic vibration was caused by its methylene groups. The FTIR signal of the methylene groups on the HG-Ni was also observed at 2973 cm^{-1}. This further supported the idea that $Ni(acac)_2$ did not decompose into Ni oxides in the conjugation procedures and that the Ni sites in HG-Ni were molecularly well-defined. The negative shift of the peak position indicated the decreased electron density in the methylene groups. These results might confirm the bonding of Ni^{2+} ions with HG. The electron distribution was thus altered in the neighboring groups of Ni^{2+} ions. From $Ni(acac)_2$ to HG-Ni, we observed a shift of Ni-to-ligand charge transfer band in the ultraviolet (UV)–visible spectra (fig. S5). This also provided support over the change of electron distribution.

Electrochemical investigations

Cyclic voltammetry (CV) of HG-Ni was conducted in 1 M KOH using common glassware as the electrochemical cell (Fig. 2A and fig. S6). In the initial scan, the HG-Ni showed a pair of redox peaks at 1.3 to 1.4 V [all potentials were quoted against the reversible hydrogen electrode (RHE) unless stated otherwise], corresponding to the typical $Ni^{2+/3+}$ couple (*36*–*38*). At higher potentials, HG-Ni delivered an insignificant OER current. Throughout the continuous CV scanning, both the currents of the $Ni^{2+/3+}$ redox and OER first increased and then stabilized

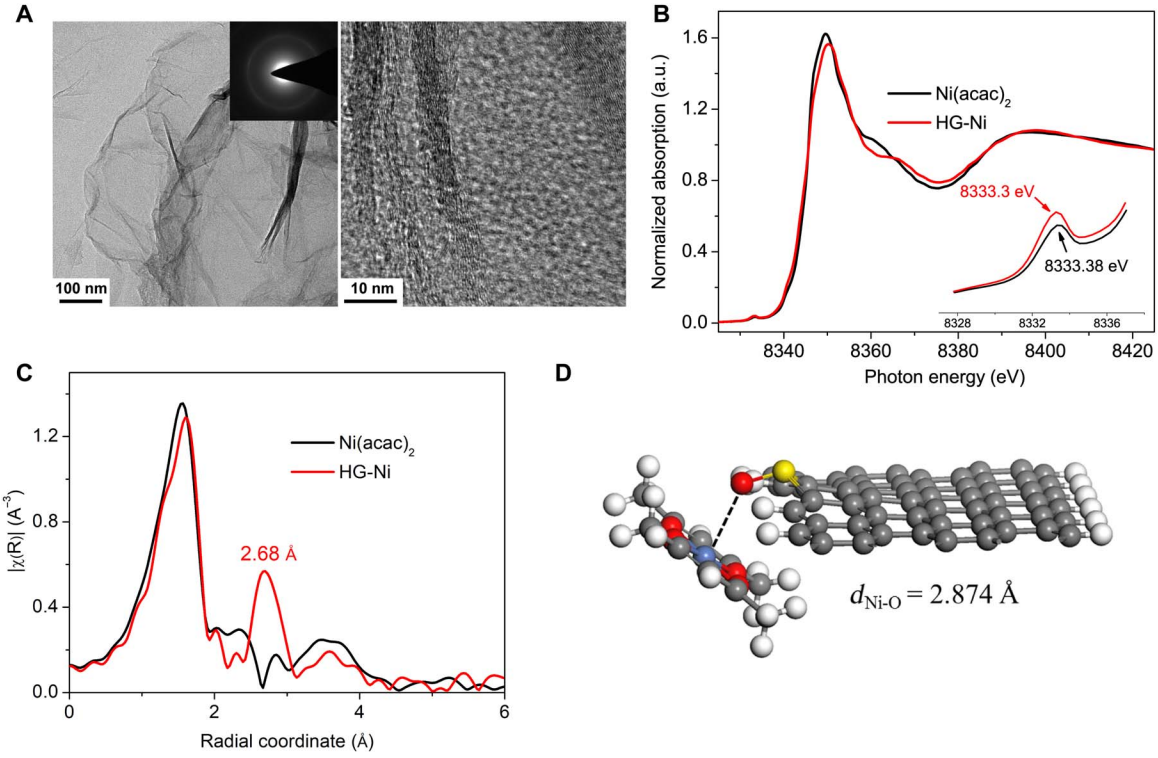

Fig. 1. Characterizations of HG-Ni. (**A**) TEM images of HG-Ni at different magnifications. (**B**) Normalized Ni K-edge XAS data of HG-Ni and $Ni(acac)_2$. The inset presents the pre-edge region. a.u., arbitrary units. (**C**) Fourier-transformed EXAFS curves at Ni K-edge. (**D**) A DFT calculation–derived model to indicate the conjugation of $Ni(acac)_2$ onto HG. The dopant of HG was a sulfoxide group as one representative interacting site. The gray, white, red, and yellow spheres represent C, H, O, and S atoms, respectively. The Ni atom is represented by a dark blue sphere.

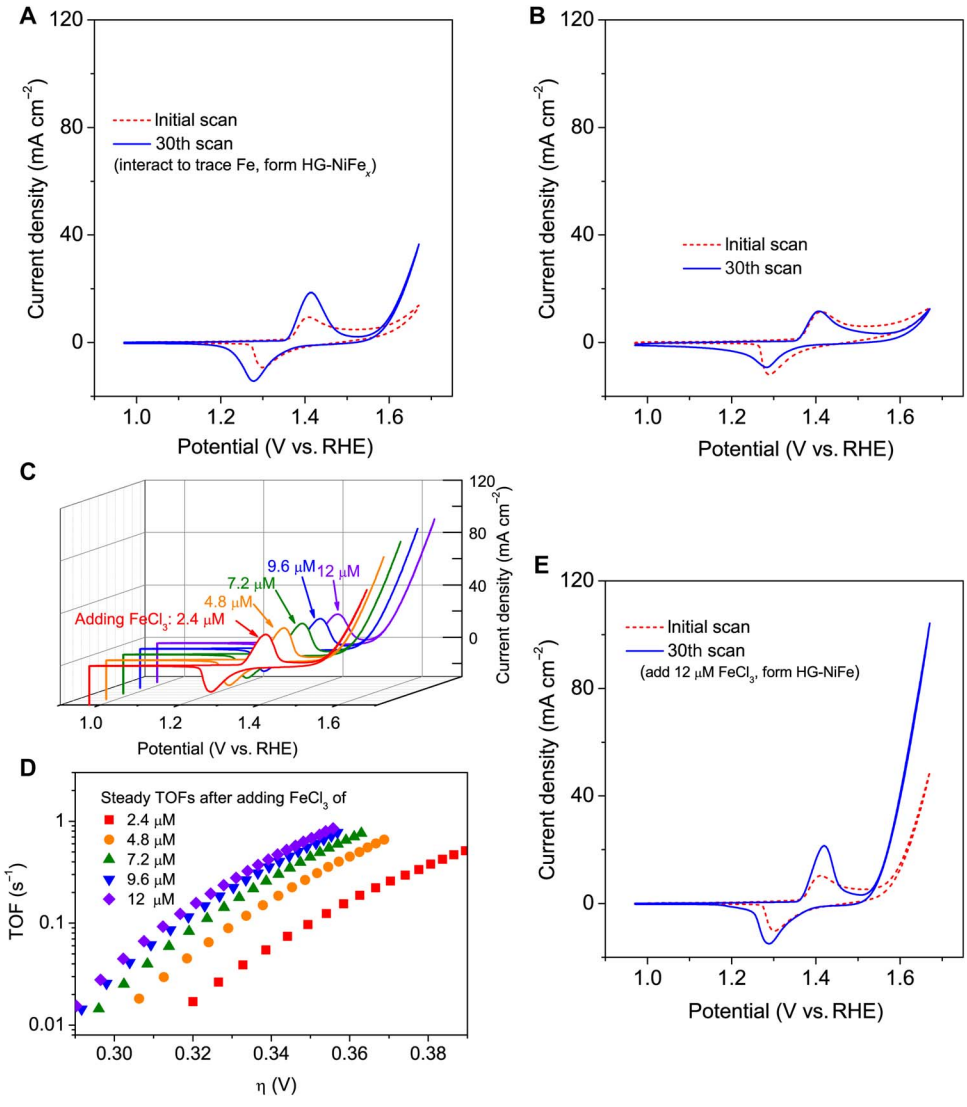

Fig. 2. Electrochemical tests of HG-Ni. CV polarization curves of HG-Ni conducted in (**A**) a glass cell, 1 M KOH without any treatment; (**B**) a plastic vessel, 1 M KOH with removal of Fe impurity. (**C**) Steady CV curves of HG-Ni performed in a glass cell in 1 M KOH solution containing different contents of $FeCl_3$ from 2.4 to 12 μM and (**D**) the corresponding TOF analysis after the potentials were compensated for *iR* drop. (**E**) Comparison of the initial and steady CV curves of HG-Ni conducted in a glass cell, 1 M KOH + 12 μM $FeCl_3$. Scan rate, 50 mV s^{-1}; rotation rate, 2000 rpm.

after 30 cycles. As previously reported, KOH solutions could etch glassware to release trace Fe species, which were reactive to some Ni-based structures, for example, $Ni(OH)_2$ and NiO (*36*, *39*). To verify whether the Fe species could interact with HG-Ni, CV of HG-Ni was conducted in a purified KOH solution without Fe species in a plastic vessel. The redox currents of $Ni^{2+/3}$ exhibited little variation, and OER currents remained small during the CV cycles (Fig. 2B). Accordingly, it was inferred that the trace Fe species of KOH solution could cause a structural evolution of HG-Ni and serve as an important determinant to OER activity. We further investigated the influence of the Fe quantity on OER activity by the stepwise addition of $FeCl_3$ to the 1 M KOH solution. As gained from the CV measurements, the addition of $FeCl_3$ clearly improved the OER activity of HG-Ni. With the increase in the content of $FeCl_3$ from 2.4 to 12 μM, the improvement was observed to be significant initially and then gradually turned to be very moderate (Fig. 2, C and D; details are provided in Materials and Methods). Therefore, we used 1 M KOH containing 12 μM $FeCl_3$ to study the structure evolution of Ni and Fe sites in the following experiments. Figure 2E presents a typical variation of OER currents on HG-Ni after continuous CV scanning in the 1 M KOH + 12 μM $FeCl_3$ solution [after reaching the steady state, the electrocatalyst on the glassy carbon electrode (GCE) was denoted as HG-NiFe; for comparison, in the case of Fig. 2A, the electrocatalyst at the steady state was denoted as HG-NiFe$_x$, which contains much less Fe]. CV of HG-NiFe was also conducted in a fresh 1 M KOH solution, and it exhibited little difference compared to the one collected in the KOH/$FeCl_3$ solution (fig. S7), suggesting that the activity comes from the heterogeneous structure. The OER products on HG-NiFe were analyzed by gas chromatography (fig. S8). O_2 was the only gaseous product and it was produced with Faradic efficiencies (FEs) of 100% at potentials from 1.54, 1.58, and 1.62, to 1.66 V. In addition, long-term measurement indicated the good stability of HG-NiFe for OER electrocatalysis (fig. S9).

To reduce the influence of metal redox and the capacitance currents of HG-NiFe on OER activity, we conducted linear scanning voltammogram

(LSV) at a low scan rate of 5 mV s^{-1} in 1 M KOH, and the *iR*-corrected polarization curve was collected (Fig. 3A). HG-NiFe afforded an OER onset potential of 1.54 V (defined as the potential at 10 mA cm^{-2}), whereas the value was 1.6 V on HG-$NiFe_x$. Correspondingly, the Tafel slope increased from 39 to 59 mV dec^{-1} (Fig. 3B). The intrinsic OER activity of HG-NiFe was determined by TOFs, which were obtained by normalizing the OER currents with electroactive metal sites (Fig. 3C). At $\eta = 0.35$ V, the TOF was calculated to be 0.53 s^{-1}, which was almost 10-fold higher than that of HG-$NiFe_x$. (For HG-Ni, it was difficult to obtain the accurate value of TOF because of the trivial OER currents. However, its TOF should be very low.) The TOF of HG-NiFe was also increased twofold compared to our previously reported molecular Co sites (0.27 s^{-1}) (*23*).

Formation of molecular Ni-Fe dual sites

The TEM images revealed the graphene structure of HG-NiFe, and the EDX results indicated the uniform distribution of Ni and Fe on the graphene layers (fig. S10). None of the Ni/Fe hydroxides (or oxides) were observed in HG-NiFe (fig. S11). The x-ray diffraction pattern showed only the graphite (002) and (111) facets (fig. S12). We also used ethylenediaminetetraacetic acid (EDTA) disodium to treat the HG-NiFe surface. EDTA is known as a strong ligand for metal cations, which should readily chelate Ni or Fe ions. After the HG-NiFe surface was immersed in 2 mM EDTA solution for 12 hours under ambient environment, the metal redox of HG-NiFe became featureless, as shown by CV measurements, and the surface was OER-inert, indicating that the metal sites were removed from HG. In UV-visible spectra, the resultant EDTA solution exhibited a weak absorption peak at 590 nm, attributed to the d-d transition of EDTA-Ni complexes. In contrast, the EDTA solution was reacted to excess bulk $Ni(OH)_2$ or $Ni(OH)_2$ nanostructures under the same conditions, where the formation of EDTA-Ni complexes is expected to be slow. The resultant solutions did not exhibit any clear absorbance of d-d transition (fig. S13). These results confirmed the incorporation of Fe into HG-Ni and indicated that the Ni-Fe sites could remain molecularly dispersed. In a control experiment, the CV measurement of the HG precursor was conducted in the 1 M KOH + 12 μM $FeCl_3$ solution for comparison. The polarization curve showed negligible OER currents. It did not exhibit any redox features for $Fe^{2+/3+}$ sites, and electrodeposition of Fe oxides/hydroxides was not observed (figs. S14 and S15) (*40*). This suggested that the Fe species cannot be directly incorporated into HG in the KOH solution. Instead, in the case of HG-Ni, the presence of Ni facilitated the incorporation of Fe species by interacting with the Ni sites, and it most likely generated molecular clusters containing the Ni-Fe dual sites.

On the basis of the normalized Ni K-edge XAS analysis, we found that there was almost no difference in the pre-edge and rising-edge positions of the Ni sites between HG-Ni and HG-NiFe (Fig. 4A). The incorporation of Fe clearly did not change the coordination geometry or the oxidation state of the Ni sites. The local structure of the Ni sites was investigated using EXAFS (Fig. 4B). The significantly increased peak was observed with R' slightly shifting around 2.71 Å. This indicated that the outer shell of the Ni centers in HG-NiFe obviously changed compared to that of HG-Ni. The normalized Fe K-edge data of HG-NiFe are presented in Fig. 4C. FeOOH and $FeCl_3$ samples were also included for comparison. In particular, the pre-edge peak of HG-NiFe showed the lowest intensity, indicating the octahedral geometry of the Fe center–based coordination. In addition, it exhibited symmetry higher than that of the Fe centers in FeOOH and $FeCl_3$ (*41*, *42*). The rising-edge energy of HG-NiFe suggested that the oxidation state of Fe sites was +3. Meanwhile, the positive shift, compared to FeOOH and $FeCl_3$, indicated a lower electron density in the Fe sites. On the basis of the EXAFS data, the local structure of the Fe centers in HG-NiFe was clearly different from those in FeOOH and $FeCl_3$ (Fig. 4D). The outer shell of the Fe centers was identified by the intense peak at R' = 2.72 Å. This is consistent with the one collected at the Ni centers, reflecting that Fe was bonded at the neighboring sites of Ni centers in HG-NiFe. The formation of dual Ni-Fe sites was also investigated by DFT calculations (fig. S16). Because the formation process was realized in the alkaline solution, we considered that a fraction of acetylacetonate ligands at Ni sites of HG-Ni might be replaced by HO^- ions. In a stable model, it was found that the O atoms of HO^- ions at Ni sites also served as the ligands coordinating to $FeCl_3$. The Ni-Fe distance in this model was calculated to be 2.73 Å, which was consistent with EXAFS results of Ni and Fe sites. In the OER process, the residual ligands on the Ni-Fe sites (acetylacetonates or chloride ions) could still be labile to provide the open sites for the further adsorption of HO^- ions as OER reactants.

Adsorption of HO^- ions at Ni-Fe sites

We investigated the adsorption of HO^- ions, which were the reactants in OER, at the Ni-Fe sites of HG-NiFe. HG-Ni and HG-$NiFe_x$ were also examined as control samples. Despite the immobilized states of Ni-Fe or Ni sites on graphene, their steady redox currents all exhibited linear dependence on the square root of potential scan rates in CVs (5 to 700 mV s^{-1}; figs. S17 to S19). This revealed that the rate-limiting step of metal redox was controlled by the mass diffusion from the electrolyte to the electrode. In alkaline solutions, the redox of Ni-Fe or Ni sites was

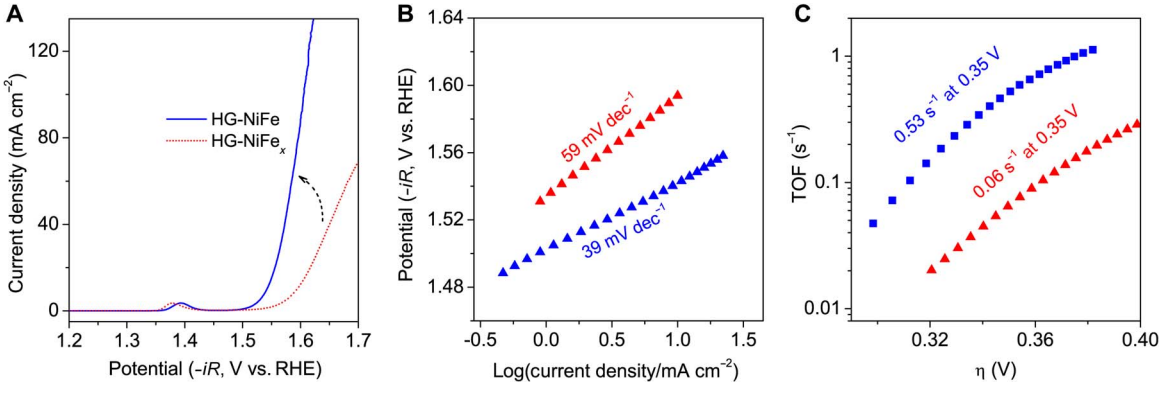

Fig. 3. OER assessments of HG-NiFes. (**A**) *iR*-compensated LSVs of HG-NiFe and HG-$NiFe_x$ in 1 M KOH (5 mV s^{-1}; 2000 rpm), corresponding Tafel slopes (**B**) and TOF analysis (**C**).

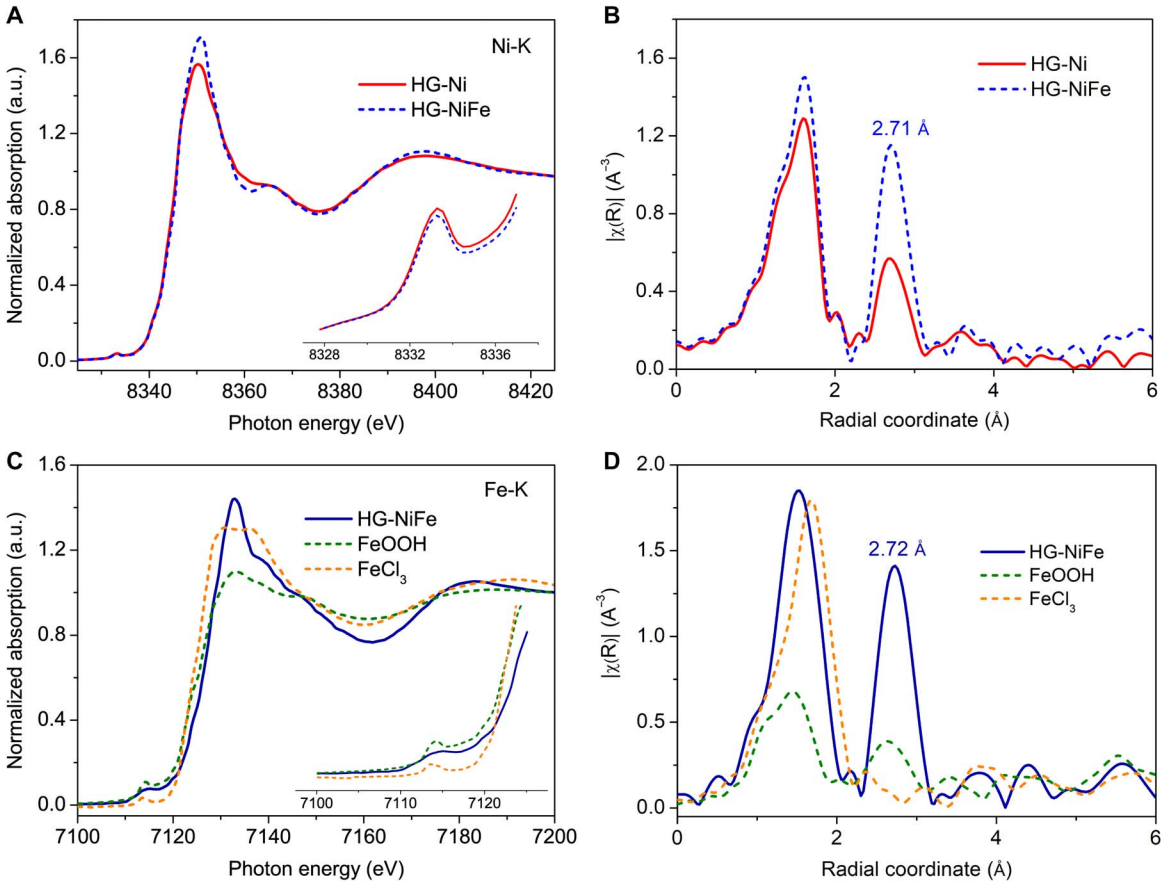

Fig. 4. Formation of molecular Ni-Fe sites. (**A**) Normalized Ni K-edge XAS data of HG-Ni and HG-NiFe. The inset presents the pre-edge region. (**B**) Fourier-transformed EXAFS curves at Ni K-edge. (**C**) Normalized Fe K-edge XAS data of HG-NiFe, FeOOH, and $FeCl_3$. (**D**) Fourier-transformed EXAFS curves at Fe K-edge.

typically coupled with the transfer of HO^- ions (*26*, *29*, *37*). The redox constants (k_s) were determined by Laviron's method (*43*). It showed that the k_s of HG-NiFe (0.79 s^{-1}) was lower than that of HG-Ni (0.92 s^{-1}), because the redox kinetics of the metal sites was determined by the diffusion of HO^- ions from electrolytes to electrodes and coupling with the metal sites. The relatively low k_s of HG-NiFe suggested that the coupling of HO^- ions with Ni-Fe sites was slower than that with Ni sites (Fig. 5A). In different KOH solutions with various pH values, the redox potentials of HG-NiFe exhibited linear dependence on pH with a slope of 0.074 V pH^{-1}, as plotted in the Pourbaix diagram (Fig. 5B). On the basis of the Nernst equation, the linear slope of 0.059 V pH^{-1} corresponded to the redox process with a HO^- (H^+)/e stoichiometry of 1; the 0.118 V pH^{-1} corresponded to a HO^- (H^+)/e stoichiometry of 2. In the present case, the medium value of 0.074 V pH^{-1} indicated that the redox process of HG-NiFe involved a HO^- (H^+)/e stoichiometry of $^3/_2$. Combining this result with the DFT-derived Ni-Fe model, we proposed that, at each Ni-Fe site in the redox process, two HO^- ions were adsorbed with terminal geometry and one HO^- ion was adsorbed with bridging geometry. This process is presented in the inset of Fig. 5B. Such a configuration was common for Ni-Fe cluster–based coordination structures, and the Ni-Fe distance (2.7 Å) in HG-NiFe was consistent with previous studies, which also involved bridging oxygen-containing ligands (*44*–*46*). Furthermore, it was also mentioned in a previous study on hydrous nickel oxides that the redox potentials of dual Ni sites with bridging oxygen-containing ligands exhibited similar linear dependence on pH (*38*). In contrast, the Pourbaix diagram of HG-Ni showed a linear slope of 0.052 V pH^{-1}, indicating that each Ni site of HG-Ni interacted with one HO^- ion by terminal geometry (fig. S20). We used CO to selectively obstruct the adsorption of HO^- ions on HG-NiFe (fig. S21). CO is a π acceptor ligand that can occupy the Ni^{2+} ions through π back-bonding (*47*, *48*). However, the Fe sites of HG-NiFe were at an oxidation state of +3 and exhibited lower electron density than that of $FeCl_3$ and FeOOH precursors, the occupation of CO is very difficult (*49*). After the HG-NiFe surface was immersed into KOH solutions with bubbling CO for 4 hours, the OER currents on the resultant HG-NiFe clearly degraded, suggesting that cooperativity between Ni and Fe sites mainly enabled the high OER activity of HG-NiFe.

Finally, during the in situ formation of Ni-Fe sites by CV measurements (Fig. 2E), it is possible that pristine molecular Ni sites of HG-Ni could aggregate into Ni hydroxides and interacted with Fe species to form Ni-Fe hydroxides at OER potentials, therefore losing the feature of molecular dispersion. To further exclude such a possibility, we presented the CV result of HG-Ni in the KOH/$FeCl_3$ solution in the absence of OER polarization (fig. S22A). The metal redox exhibited a similar variation to that presented in Fig. 2E. After reaching the steady state, the LSV of the electrode was collected at a scan rate of 5 mV s^{-1}, affording an OER onset potential of 1.55 V and a TOF of 0.57 s^{-1} at η = 0.35 V (fig. S22B). Moreover, the redox currents of the metal sites exhibited linear dependence on the square root of potential scan rates, indicating that the diffusion of HO^- ions was the rate-limiting step, and k_s was calculated to be 0.75 s^{-1} (fig. S23). All these OER results were consistent with those collected on HG-NiFe.

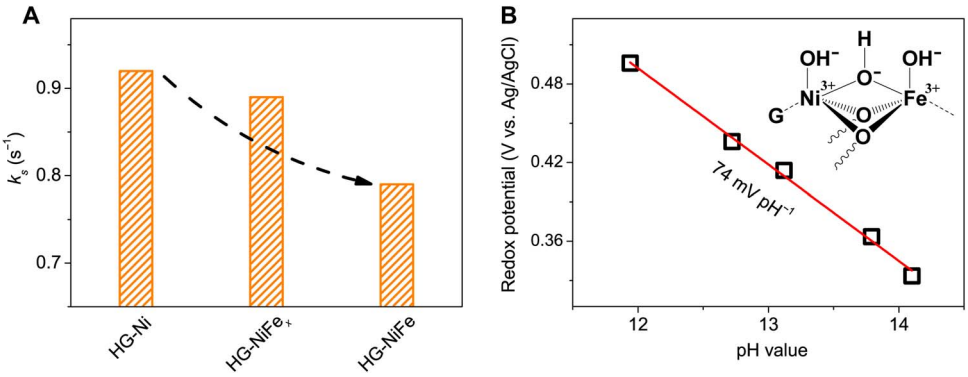

Fig. 5. Adsorption of HO^- ions at Ni-Fe sites. (**A**) k_s of metal redox in HG-Ni, HG-NiFe$_x$, and HG-NiFe. (**B**) Pourbaix diagram, formal potentials of redox versus pH values of KOH solutions. The inset shows the proposed configuration for the adsorption of HO^- ions onto Ni-Fe sites before OER.

DISCUSSION

In summary, we have reported that Ni^{2+} ions were incorporated into HG under mild conditions to form heterogeneous and molecularly well-defined Ni sites for OER in alkaline aqueous solutions. The molecular Ni sites on graphene were intrinsically not OER-active. However, they could interact with Fe species in KOH solutions to form Ni-Fe sites. This structural variation resulted in a significant enhancement on OER activity. The structure of Ni-Fe sites was investigated by various techniques. The results showed that they maintained molecular dispersion on graphene, and the Ni-Fe distance was revealed to be 2.7 Å. We also proposed that the adsorption configuration with HO^- ions was tuned from pristine Ni sites to Ni-Fe sites. HO^- ions were bridged with the Ni-Fe sites before OER. These results demonstrated a novel, molecularly well-defined and heterogeneous structure catalyst for OER which might also serve as a platform to gain further insights into the OER mechanism.

MATERIALS AND METHODS

Chemicals

Graphite powders, thiourea, KOH, $K_2S_2O_8$, P_2O_5, $KMnO_4$, $Ni(acac)_2$, $Fe(acac)_3$, and $FeCl_3{\cdot}6H_2O$ were purchased from Sigma-Aldrich and used as received. Other reagents and solvents were of analytical or high-performance liquid chromatography grade and used without further purification. All aqueous solutions were prepared with Millipore water with a resistivity of 18 megohm·cm.

Synthesis of HG-Ni

Graphene oxides (GOs) were synthesized following a modified Hummers' method, as previously established (*23*). An aqueous suspension of GO (1 mg ml^{-1}, 10 ml) was mixed with thiourea at a mass ratio of 1:50 (GO/thiourea), followed by sealing in a Teflon-lined stainless autoclave at 150°C for 3 hours to obtain HG. Afterward, the as-obtained HG [6 to 7 mg; dispersed in 10 ml of *N*,*N*-dimethylformamide (DMF)] was mixed with 0.1 M $Ni(acac)_2$ (dissolved in 10 ml of DMF) at 80°C for 12 hours (1 atm) to form HG-Ni. The resultant HG-Ni was dispersed and stored in isopropanol with a concentration of 1 mg ml^{-1}. In a control experiment, we used the same procedure to synthesize an HG-Fe sample. In particular, HG (6 to 7 mg; in 10 ml of DMF) was mixed with 0.1 M $Fe(acac)_3$ (dissolved in 10 ml of DMF) at 80°C for 12 hours (1 atm).

Electrochemical measurements

All electrochemical measurements were performed on an Autolab PGSTAT302 potentiostat at ambient environment (23° ± 1°C, 1 atm). Electrocatalysts were casted onto rotating GCEs (4 mm in diameter; typically loaded with 10 μl of 1 mg ml^{-1} of HG-Ni) as working electrodes and attached to a Pine Instruments MSR rotator. An Ag/AgCl wire (placed in saturated KCl solution that was periodically refreshed to counteract the contamination from electrolytes) was used as the reference electrode, and a Pt foil was used as the counter electrode. The potential of the Ag/AgCl reference electrode was converted to a RHE scale following the equation E (RHE) = E (Ag/AgCl) + 0.059 pH (KOH solutions) V. The alternating current (ac) impedance measurement for *iR* compensation (95%) to OER currents was performed at η = ~0.35 V from 10^5 to −0.1 Hz with an ac voltage of 5 mV. The gaseous products of OER were analyzed by gas chromatography. Typically, the OER measurement was conducted in 1 M KOH in an H-type cell with the cathode (Pt foil) and the anode (HG-NiFe– or HG-NiFe$_x$–coated carbon papers, and the anodic chamber contained a Ag/AgCl reference electrode) separated by a membrane. During electrolysis, helium was continuously sparged into the anodic chamber with a flow rate of 20 standard cubic centimeters per minute. The gaseous product from the anode was measured in real time by in-line gas chromatography. On HG-NiFe, O_2 was the only product and it was produced with FEs of 100% at potentials from 1.54, 1.58, 1.62, to 1.66 V. On HG-NiFe$_x$, the FEs for O_2 production were also 100% at 1.62, 1.66, and 1.70 V.

Removal of Fe species from KOH solutions

KOH solutions (in this case, the Fe content in the raw KOH solution was detected by inductively coupled plasma measurements, but it suggested that the Fe content should be at a trace level) were purified following a previously reported approach (*36*). Briefly, 2 g of Ni $(NO_3)_2{\cdot}6H_2O$ was mixed with 20 ml of 1 M KOH in polypropylene centrifuge tubes to achieve $Ni(OH)_2$ solids, followed by washing with Millipore water and 1 M KOH successively. Afterward, 40 ml of 1 M KOH was added to mix with the $Ni(OH)_2$ solids in the polypropylene centrifuge tubes for 4 to 5 hours. In the electrochemical measurement, the purified 1 M KOH was stored in a plastic beaker.

Procedures to obtain HG-NiFe

In a typical experiment, 10 μl of HG-Ni (1 mg ml^{-1}) was casted onto GCE. The CV of HG-Ni/GCE was performed in 30 ml of 1 M KOH at a scan rate of 50 mV s^{-1}. During this process, 200 μl of $FeCl_3$ aqueous solution (1.8 mM in water) was injected stepwise into the KOH solution. The CV polarization curve can reach steady state after 30 cycles. In a control experiment, 10 μl of HG suspension (1 mg ml^{-1}) was casted on

GCE and underwent the same procedure to investigate the interacting sites of HG-Ni with the Fe species.

Calculation of TOFs

$$\mathrm{TOF} = (J \times A)/(4 \times F \times m) \quad (1)$$

where J is the OER current density, which was achieved from LSV with a low scan rate of 5 mV s^{-1} to minimize the influence of the currents from metal redox and electrode capacitance; A is the geometrical surface area of the electrode; F is the Faraday constant; and m is the amount of electroactive Ni or Ni-Fe sites, which was obtained from integrating the charge amount of metal redox peaks.

Laviron equation

$$E_c = E_{1/2} - (RT/\alpha nF) \times \ln(\alpha nF/RTk_s) - (RT/\alpha nF) \times \ln(v) \quad (2)$$

where E_c is the reduction potential of metal redox, $E_{1/2}$ is the formal potential of metal redox, R is the universal gas constant, T is the temperature in kelvin, n is the number of electrons transferred, α is the transfer coefficient, k_s is the rate constant of metal redox, and v is the scan rate in the CV measurements (*43*).

Computational method

Our calculations were performed based on DFT implemented in the QUANTUM-ESPRESSO package (*50*). Structural relaxation was performed by using spin-polarized scalar relativistic ultrasoft pseudopotentials and an exchange correlation functional in the form of a Perdew-Burke-Ernzerhof functional with the van der Waals interaction by the empirical dispersion correction. Vacuum regions of at least 20 and 15 Å in vertical and parallel directions, respectively, were applied to avoid unphysical interactions between periodic images. All calculations were conducted with a plane wave cutoff of 60 rydberg and a $1 \times 3 \times 1$ Monkhorst-Pack k-grid for the Brillouin zone (*51*), which are sufficient to ensure convergence. Geometry optimization was performed using a quasi-Newton algorithm. A total energy convergence of 1.4×10^{-4} eV and residual forces below 0.02 eV $Å^{-1}$ were achieved.

SUPPLEMENTARY MATERIALS

Supplementary material for this article is available at http://advances.sciencemag.org/cgi/content/full/4/3/eaap7970/DC1

fig. S1. High-resolution TEM images of HG-Ni.
fig. S2. SEM image of HG-Ni with EDX analysis.
fig. S3. TEM image of HG-Ni with EDX analysis.
fig. S4. FTIR spectra of $Ni(acac)_2$, HG, and HG-Ni.
fig. S5. UV-visible spectra of $Ni(acac)_2$, HG, and HG-Ni.
fig. S6. Schematic illustrations of electrochemical tests.
fig. S7. CVs of HG-NiFe in 1 M KOH before and after removal of $FeCl_3$.
fig. S8. GC spectrum of O_2 detection.
fig. S9. OER durability on HG-NiFe.
fig. S10. TEM image of HG-NiFe with EDX analysis.
fig. S11. TEM images of HG-NiFe.
fig. S12. XRD patterns of HG, HG-Ni, and HG-NiFe.
fig. S13. EDTA treatment of HG-NiFe.
fig. S14. CVs of HG in 1 M KOH containing $FeCl_3$.
fig. S15. Comparisons of CVs of HG-NiFe and HG-Fe.
fig. S16. DFT model of Ni-Fe sites.
fig. S17. Analysis of HG-NiFe in Laviron equation.
fig. S18. Analysis of HG-$NiFe_x$ in Laviron equation.
fig. S19. Analysis of HG-Ni in Laviron equation.
fig. S20. Pourbaix diagram of HG-Ni.
fig. S21. CO poisoning of HG-NiFe.
fig. S22. CV and TOF analysis of a control sample.
fig. S23. Analysis of a control sample in Laviron equation.

REFERENCES AND NOTES

1. I. Roger, M. A. Shipman, M. D. Symes, Earth-abundant catalysts for electrochemical and photoelectrochemical water splitting. *Nat. Rev. Chem.* **1**, 0003 (2017).
2. B. M. Hunter, H. B. Gray, A. M. Müller, Earth-abundant heterogeneous water oxidation catalysts. *Chem. Rev.* **116**, 14120–14136 (2016).
3. C. Liu, N. P. Dasgupta, P. Yang, Semiconductor nanowires for artificial photosynthesis. *Chem. Mater.* **26**, 415–422 (2014).
4. Y. Lee, J. Suntivich, K. J. May, E. E. Perry, Y. Shao-Horn, Synthesis and activities of rutile IrO_2 and RuO_2 nanoparticles for oxygen evolution in acid and alkaline solutions. *J. Phys. Chem. Lett.* **3**, 399–404 (2012).
5. J. Rossmeisl, Z.-W. Qu, H. Zhu, G.-J. Kroes, J. K. Nørskov, Electrolysis of water on oxide surfaces. *J. Electroanal. Chem.* **607**, 83–89 (2007).
6. J. D. Blakemore, R. H. Crabtree, G. W. Brudvig, Molecular catalysts for water oxidation. *Chem. Rev.* **115**, 12974–13005 (2015).
7. E. Mirzakulova, R. Khatmullin, J. Walpita, T. Corrigan, N. M. Vargas-Barbosa, S. Vyas, S. Oottikkal, S. F. Manzer, C. M. Hadad, K. D. Glusac, Electrode-assisted catalytic water oxidation by a flavin derivative. *Nat. Chem.* **4**, 794–801 (2012).
8. M. D. Kärkäs, O. Verho, E. V. Johnston, B. Åkermark, Artificial photosynthesis: Molecular systems for catalytic water oxidation. *Chem. Rev.* **114**, 11863–12001 (2014).
9. E. Y. Tsui, R. Tran, J. Yano, T. Agapie, Redox-inactive metals modulate the reduction potential in heterometallic manganese–oxido clusters. *Nat. Chem.* **5**, 293–299 (2013).
10. S. Bang, Y.-M. Lee, S. Hong, K.-B. Cho, Y. Nishida, M. S. Seo, R. Sarangi, S. Fukuzumi, W. Nam, Redox-inactive metal ions modulate the reactivity and oxygen release of mononuclear non-haem iron(III)–peroxo complexes. *Nat. Chem.* **6**, 934–940 (2014).
11. T. Fukushima, W. Drisdell, J. Yano, Y. Surendranath, Graphite-conjugated pyrazines as molecularly tunable heterogeneous electrocatalysts. *J. Am. Chem. Soc.* **137**, 10926–10929 (2015).
12. C. M. Araujo, M. D. Doherty, S. J. Konezny, O. R. Luca, A. Usyatinsky, H. Grade, E. Lobkovsky, G. L. Soloveichik, R. H. Crabtree, V. S. Batista, Tuning redox potentials of bis(imino)pyridine cobalt complexes: An experimental and theoretical study involving solvent and ligand effects. *Dalton Trans.* **41**, 3562–3573 (2012).
13. D. J. Cole-Hamilton, Homogeneous catalysis—New approaches to catalyst separation, recovery, and recycling. *Science* **299**, 1702–1706 (2003).
14. A. Choplin, F. Quignard, From supported homogeneous catalysts to heterogeneous molecular catalysts. *Coord. Chem. Rev.* **178–180** (Pt. 2), 1679–1702 (1998).
15. J. R. McKone, N. S. Lewis, H. B. Gray, Will solar-driven water-splitting devices see the light of day? *Chem. Mater.* **26**, 407–414 (2014).
16. S. Lin, C. S. Diercks, Y.-B. Zhang, N. Kornienko, E. M. Nichols, Y. Zhao, A. R. Paris, D. Kim, P. Yang, O. M. Yaghi, C. J. Chang, D. Kim, Covalent organic frameworks comprising cobalt porphyrins for catalytic CO_2 reduction in water. *Science* **349**, 1208–1213 (2015).
17. E. S. Andreiadis, P.-A. Jacques, P. D. Tran, A. Leyris, M. Chavarot-Kerlidou, B. Jousselme, M. Matheron, J. Pécaut, S. Palacin, M. Fontecave, V. Artero, Molecular engineering of a cobalt-based electrocatalytic nanomaterial for H_2 evolution under fully aqueous conditions. *Nat. Chem.* **5**, 48–53 (2013).
18. A. Le Goff, V. Artero, B. Jousselme, P. D. Tran, N. Guillet, R. Métayé, A. Fihri, S. Palacin, M. Fontecave, From hydrogenases to noble metal-free catalytic nanomaterials for H_2 production and uptake. *Science* **326**, 1384–1387 (2009).
19. J. D. Blakemore, A. Gupta, J. J. Warren, B. S. Brunschwig, H. B. Gray, Noncovalent immobilization of electrocatalysts on carbon electrodes for fuel production. *J. Am. Chem. Soc.* **135**, 18288–18291 (2013).
20. P. D. Tran, A. Le Goff, J. Heidkamp, B. Jousselme, N. Guillet, S. Palacin, H. Dau, M. Fontecave, V. Artero, Noncovalent modification of carbon nanotubes with pyrene-functionalized nickel complexes: Carbon monoxide tolerant catalysts for hydrogen evolution and uptake. *Angew. Chem. Int. Ed.* **50**, 1371–1374 (2011).
21. X. Zhang, Z. Wu, X. Zhang, L. Li, Y. Li, H. Xu, X. Li, X. Yu, Z. Zhang, Y. Liang, H. Wang, Highly selective and active CO_2 reduction electrocatalysts based on cobalt phthalocyanine/carbon nanotube hybrid structures. *Nat. Commun.* **8**, 14675 (2017).
22. K. Elouarzaki, A. Le Goff, M. Holzinger, J. Thery, S. Cosnier, Electrocatalytic oxidation of glucose by rhodium porphyrin-functionalized MWCNT electrodes: Application to a fully molecular catalyst-based glucose/O_2 fuel cell. *J. Am. Chem. Soc.* **134**, 14078–14085 (2012).
23. J. Wang, X. Ge, Z. Liu, L. Thia, Y. Yan, W. Xiao, X. Wang, Heterogeneous electrocatalyst with molecular cobalt ions serving as the center of active sites. *J. Am. Chem. Soc.* **139**, 1878–1884 (2017).
24. J. Y. C. Chen, L. Dang, H. Liang, W. Bi, J. B. Gerken, S. Jin, E. E. Alp, S. S. Stahl, Operando analysis of NiFe and Fe oxyhydroxide electrocatalysts for water oxidation: Detection of Fe^{4+} by Mössbauer spectroscopy. *J. Am. Chem. Soc.* **137**, 15090–15093 (2015).

25. M. Görlin, P. Chernev, J. Ferreira de Araújo, T. Reier, S. Dresp, B. Paul, R. Krähnert, H. Dau, P. Strasser, Oxygen evolution reaction dynamics, faradaic charge efficiency, and the active metal redox states of Ni–Fe oxide water splitting electrocatalysts. *J. Am. Chem. Soc.* **138**, 5603–5614 (2016).
26. M. Görlin, J. Ferreira de Araújo, H. Schmies, D. Bernsmeier, S. Dresp, M. Gliech, Z. Jusys, P. Chernev, R. Kraehnert, H. Dau, P. Strasser, Tracking catalyst redox states and reaction dynamics in Ni–Fe oxyhydroxide oxygen evolution reaction electrocatalysts: The role of catalyst support and electrolyte pH. *J. Am. Chem. Soc.* **139**, 2070–2082 (2017).
27. D. Friebel, M. W. Louie, M. Bajdich, K. E. Sanwald, Y. Cai, A. M. Wise, M.-J. Cheng, D. Sokaras, T.-C. Weng, R. Alonso-Mori, R. C. Davis, J. R. Bargar, J. K. Nørskov, A. Nilsson, A. T. Bell, Identification of highly active Fe sites in (Ni,Fe)OOH for electrocatalytic water splitting. *J. Am. Chem. Soc.* **137**, 1305–1313 (2015).
28. M. Gong, Y. Li, H. Wang, Y. Liang, J. Z. Wu, J. Zhou, J. Wang, T. Regier, F. Wei, H. Dai, An advanced Ni–Fe layered double hydroxide electrocatalyst for water oxidation. *J. Am. Chem. Soc.* **135**, 8452–8455 (2013).
29. C. Yang, O. Fontaine, J.-M. Tarascon, A. Grimaud, Chemical recognition of active oxygen species on the surface of oxygen evolution reaction electrocatalysts. *Angew. Chem. Int. Ed.* **56**, 8652–8656 (2017).
30. X. Xu, F. Song, X. Hu, A nickel iron diselenide-derived efficient oxygen-evolution catalyst. *Nat. Commun.* **7**, 12324 (2016).
31. X. Lu, C. Zhao, Electrodeposition of hierarchically structured three-dimensional nickel–iron electrodes for efficient oxygen evolution at high current densities. *Nat. Commun.* **6**, 6616 (2015).
32. G. J. Colpas, M. J. Maroney, C. Bagyinka, M. Kumar, W. S. Willis, S. L. Suib, P. K. Mascharak, N. Baidya, X-ray spectroscopic studies of nickel complexes, with application to the structure of nickel sites in hydrogenases. *Inorg. Chem.* **30**, 920–928 (1991).
33. Y. Tian, B. Etschmann, W. Liu, S. Borg, Y. Mei, D. Testemale, B. O'Neill, N. Rae, D. M. Sherman, Y. Ngothai, B. Johannessen, C. Glover, J. Brugger, Speciation of nickel (II) chloride complexes in hydrothermal fluids: In situ XAS study. *Chem. Geol.* **334**, 345–363 (2012).
34. M. B. Hursthouse, M. A. Laffey, P. T. Moore, D. B. New, P. R. Raithby, P. Thornton, Crystal and molecular structures of some binuclear complexes of cobalt(II) and nickel(II) acetylacetonates with pyridines and piperidine and a refinement of the crystal and molecular structure of hexakis-(acetylacetonato)trinickel(II). *J. Chem. Soc. Dalton Trans.*, 307–312 (1982).
35. R. Sarangi, X-ray absorption near-edge spectroscopy in bioinorganic chemistry: Application to M–O_2 systems. *Coord. Chem. Rev.* **257**, 459–472 (2013).
36. L. Trotochaud, S. L. Young, J. K. Ranney, S. W. Boettcher, Nickel–iron oxyhydroxide oxygen-evolution electrocatalysts: The role of intentional and incidental iron incorporation. *J. Am. Chem. Soc.* **136**, 6744–6753 (2014).
37. M. W. Louie, A. T. Bell, An investigation of thin-film Ni–Fe oxide catalysts for the electrochemical evolution of oxygen. *J. Am. Chem. Soc.* **135**, 12329–12337 (2013).
38. M. E. G. Lyons, R. L. Doyle, I. Godwin, M. O'Brien, L. Russell, Hydrous nickel oxide: Redox switching and the oxygen evolution reaction in aqueous alkaline solution. *J. Electrochem. Soc.* **159**, H932–H944 (2012).
39. B. Mei, A. A. Permyakova, R. Frydendal, D. Bae, T. Pedersen, P. Malacrida, O. Hansen, I. E. L. Stephens, P. C. K. Vesborg, B. Seger, I. Chorkendorff, Iron-treated NiO as a highly transparent p-type protection layer for efficient Si-based photoanodes. *J. Phys. Chem. Lett.* **5**, 3456–3461 (2014).
40. M. E. G. Lyons, R. L. Doyle, M. P. Brandon, Redox switching and oxygen evolution at oxidized metal and metal oxide electrodes: Iron in base. *Phys. Chem. Chem. Phys.* **13**, 21530–21551 (2011).
41. S. A. Wilson, J. Chen, S. Hong, Y.-M. Lee, M. Clémancey, R. Garcia-Serres, T. Nomura, T. Ogura, J.-M. Latour, B. Hedman, K. O. Hodgson, W. Nam, E. I. Solomon, $[Fe^{IV}{=}O(TBC)(CH_3CN)]^{2+}$: Comparative reactivity of iron(IV)-oxo species with constrained equatorial cyclam ligation. *J. Am. Chem. Soc.* **134**, 11791–11806 (2012).
42. M. Wilke, F. Farges, P.-E. Petit, E. Brown Gordon Jr., F. Martin, Oxidation state and coordination of Fe in minerals: An Fe K-XANES spectroscopic study. *Am. Mineral.* **86**, 714–730 (2001).
43. E. Laviron, The use of linear potential sweep voltammetry and of a.c. voltammetry for the study of the surface electrochemical reaction of strongly adsorbed systems and of redox modified electrodes. *J. Electroanal. Chem.* **100**, 263–270 (1979).
44. B. E. Barton, C. M. Whaley, T. B. Rauchfuss, D. L. Gray, Nickel–iron dithiolato hydrides relevant to the [NiFe]-hydrogenase active site. *J. Am. Chem. Soc.* **131**, 6942–6943 (2009).
45. S. Canaguier, V. Artero, M. Fontecave, Modelling NiFe hydrogenases: Nickel-based electrocatalysts for hydrogen production. *Dalton Trans.*, 315–325 (2008).
46. X. Engelmann, S. Yao, E. R. Farquhar, T. Szilvási, U. Kuhlmann, P. Hildebrandt, M. Driess, K. Ray, A new domain of reactivity for high-valent dinuclear $[M(\mu\text{-}O)_2M']$ complexes in oxidation reactions. *Angew. Chem. Int. Ed.* **56**, 297–301 (2017).
47. J.-H. Jeoung, H. Dobbek, Carbon dioxide activation at the Ni,Fe-cluster of anaerobic carbon monoxide dehydrogenase. *Science* **318**, 1461–1464 (2007).
48. H. Ogata, Y. Mizoguchi, N. Mizuno, K. Miki, S.-i. Adachi, N. Yasuoka, T. Yagi, O. Yamauchi, S. Hirota, Y. Higuchi, Structural studies of the carbon monoxide complex of [NiFe] hydrogenase from *Desulfovibrio vulgaris* Miyazaki F: Suggestion for the initial activation site for dihydrogen. *J. Am. Chem. Soc.* **124**, 11628–11635 (2002).
49. J. Li, B. C. Noll, C. E. Schulz, W. R. Scheidt, Comparison of cyanide and carbon monoxide as ligands in iron(II) porphyrinates. *Angew. Chem. Int. Ed.* **48**, 5010–5013 (2009).
50. P. Giannozzi, S. Baroni, N. Bonini, M. Calandra, R. Car, C. Cavazzoni, D. Ceresoli, G. L. Chiarotti, M. Cococcioni, I. Dabo, A. Dal Corso, S. de Gironcoli, S. Fabris, G. Fratesi, R. Gebauer, U. Gerstmann, C. Gougoussis, A. Kokalj, M. Lazzeri, L. Martin-Samos, N. Marzari, F. Mauri, R. Mazzarello, S. Paolini, A. Pasquarello, L. Paulatto, C. Sbraccia, S. Scandolo, G. Sclauzero, A. P. Seitsonen, A. Smogunov, P. Umari, R. M. Wentzcovitch, QUANTUM ESPRESSO: A modular and open-source software project for quantum simulations of materials. *J. Phys. Condens. Matter* **21**, 395502 (2009).
51. H. J. Monkhorst, J. D. Pack, Special points for Brillouin-zone integrations. *Phys. Rev. B* **13**, 5188–5192 (1976).

Acknowledgments: We thank the Shanghai Synchrotron Radiation Facility for providing beamline time and for supporting our XAS analysis. **Funding:** This project was funded by the National Research Foundation, Prime Minister's Office, Singapore, under its Campus for Research Excellence and Technological Enterprise program. We acknowledge financial support from the academic research fund AcRF tier 2 (M4020246, ARC10/15) of the Ministry of Education, Singapore, and a start-up grant (M4081887) from the College of Engineering, Nanyang Technological University, Singapore. **Author contributions:** X.W. conceived and supervised the project. J.W. carried out the synthesis and electrocatalytic measurements. X.W., J.W., and W.Z. co-wrote the manuscript. L.G. performed the DFT calculations. Y.P., H.Y., Q.Y., and X.X. helped with materials characterization and analysis. All authors discussed the results and commented on the manuscript. **Competing interests:** The authors declare that they have no competing interests. **Data and materials availability:** All data needed to evaluate the conclusions in the paper are present in the paper and/or the Supplementary Materials. Additional data related to this paper may be requested from X.W.

Submitted 28 August 2017
Accepted 2 February 2018
Published 9 March 2018
10.1126/sciadv.aap7970

Citation: J. Wang, L. Gan, W. Zhang, Y. Peng, H. Yu, Q. Yan, X. Xia, X. Wang, In situ formation of molecular Ni-Fe active sites on heteroatom-doped graphene as a heterogeneous electrocatalyst toward oxygen evolution. *Sci. Adv.* **4**, eaap7970 (2018).

Science Advances

In situ formation of molecular Ni-Fe active sites on heteroatom-doped graphene as a heterogeneous electrocatalyst toward oxygen evolution

Jiong Wang, Liyong Gan, Wenyu Zhang, Yuecheng Peng, Hong Yu, Qingyu Yan, Xinghua Xia and Xin Wang

Sci Adv **4** (3), eaap7970.
DOI: 10.1126/sciadv.aap7970